INORGANIC CHEMISTRY FRONTIERS

RESEARCH ARTICLE

View Article Online
View Journal | View Issue

Cite this: *Inorg. Chem. Front.*, 2025, **12**, 8785

Plasmonic Pd nanoparticles at the electrode-semiconductor interface enhance the activity of bismuth vanadate for solar-driven glycerol oxidation

Junjie Xie, [a] Brian Tam, [a,b] YiChao Cai,[b] Longren Li,[b] Zhipeng Lin,[b] Kaat Lambrecht,[b] Artem A. Bakulin *[a,b] and Andreas Kafizas *[a,b]

This study demonstrates that the integration of plasmonic palladium (Pd) nanoparticles between a bismuth vanadate (BVO) coating and an electrode interface can significantly improve solar-driven glycerol oxidation. Pd nanoparticles of controllable shape, size and coverage were produced using a novel aerosol-assisted chemical vapour deposition (AACVD) synthetic route and then coated with BVO using the same technique. The nanoparticles enhanced visible light absorption and crystallinity. At 1.23 V_{RHE}, the photocurrent density of bare BVO increased from 0.62 mA cm^{-2} in the absence of glycerol to 1.20 mA cm^{-2} with 0.5 M glycerol. When Pd nanoparticles were incorporated beneath BVO, the photocurrent further increased from 0.86 mA cm^{-2} without glycerol to 1.58 mA cm^{-2} with 0.5 M glycerol, and the incident photon-to-current conversion efficiency (IPCE) boosted from ~15% to ~40% at 400 nm. Ultra-fast transient absorption spectroscopy suggests that the addition of Pd nanoparticles introduces additional charge transfer pathways, including hot electron injection and plasmon-coupled states, which prolong carrier lifetimes and suppress recombination. These combined effects provide a promising strategy to improve the efficiency and durability of photoelectrochemical devices for sustainable fuel generation and selective organic oxidation reactions.

Received 21st July 2025,
Accepted 15th September 2025

DOI: 10.1039/d5qi01542a

rsc.li/frontiers-inorganic

1. Introduction

The growing global economy and population have increasing energy demands, where our reliance on fossil fuels is causing the climate crisis.[1–3] Given the limited nature of fossil fuel reserves, solar energy offers an alternative with vast potential to meet our global demands.[4,5] Hydrogen is a clean energy carrier that can be produced through solar-driven water splitting, offering a renewable and readily-storable solution.[6,7] Photoelectrochemical (PEC) water splitting, utilizing bulk semiconductor photoelectrodes, is one of the most promising methods for producing solar hydrogen in terms of efficiency and cost.[8] Of the various earth-abundant semiconductors investigated for use in photoelectrodes, bismuth vanadate (BVO) has emerged as a highly promising candidate due to its visible light bandgap (2.4 eV) and favourable band alignment for water oxidation,[9] chemical stability, and the potential for performance improvement through modifications such as heterojunction formation,[10–14] coupling with cocatalysts,[15–17] and introducing plasmonic metals.[18–20] However, unmodified BVO suffers from a short hole-diffusion length (<70 nm), resulting in inefficient charge separation, slow charge transport kinetics, and rapid charge recombination, ultimately leading to low activity.[14,21–23]

An emerging strategy to enhance the light absorption and charge separation in BVO photoanodes is to incorporate plasmonic metal nanoparticles (NPs), such as Au, Ag, Pt, or Pd.[24–27] While Au and Ag have been the most commonly investigated plasmonic metal NPs,[28] Pd has recently gained attention due to its broad-band light absorption capability (spanning from 200 to 1000 nm), which can improve light harvesting across the whole visible light spectrum.[27,29] Additionally, its relatively large Fermi level of 5.12 V *vs.* vacuum[30] compared to near 4.44 V *vs.* vacuum for highly n-doped BVO facilitates the formation of a Schottky barrier at the metal–semiconductor interface, potentially increasing charge separation efficiency and extending carrier lifetimes.[31] In the context of Pd/BVO systems, many studies have focused on applications such as wastewater treatment,[32,33] CO_2 reduction,[34] and water splitting,[20,25,35] where Pd mainly served as a catalytic site to facilitate redox reactions rather than as a plasmonic sensitizer.

[a]*Centre for Processable Electronics, Imperial College London, UK.*
E-mail: a.bakulin@imperial.ac.uk, a.kafizas@imperial.ac.uk
[b]*Department of Chemistry, Imperial College London, UK*

A related report demonstrated plasmonic Pd nanoparticle- and nanorod-decorated BVO electrodes with enhanced PEC activity across the visible-NIR region.[25] However, Pd directly decorated on BVO is unstable under anodic bias, where it can be readily oxidized and deactivated.[36] These properties make Pd a promising plasmonic metal for coupling with BVO photoanodes, although its practical application requires strategies to overcome stability challenges under bias to fully retain its plasmonic functionality. Herein, we show how Pd nanoparticles grown beneath BVO overlayers protect them from anodic oxidation, whilst facilitating enhanced PEC activity.

Pd induced plasmonic behaviour could involve several key stages and timescales. Upon light excitation, surface plasmon polaritons (SPPs) and localized surface plasmon resonance (LSPR) are generated, with coherent oscillations lasting around 10 femtoseconds (fs). These oscillations dephase, leading to electron–electron scattering at 100 fs, generating hot electrons.[37–39] By around 1 picosecond (ps), electron–phonon coupling occurs. Energy can be transferred to a semiconductor either through plasmon resonance energy transfer (PRET) or *via* plasmonic hot electron transfer (PIHET),[40,41] with direct interfacial charge transfer (DICTT) offering an alternative, bypassing metal relaxation processes.[41–43] Transient absorption spectroscopy (TAS) can be used to study the charge carrier dynamics in BVO and plasmonic systems.[44,45] Data from ultrafast TAS on the fs timescale[46] are typically analysed using kinetic fitting or global analysis methods, such as genetic algorithms, to resolve charge transfer processes.[47,48] In addition to these ultrafast relaxation dynamics, the strong near-field electromagnetic enhancement associated with LSPR also plays a key role in promoting interfacial charge separation. The enhanced local field increases light absorption in the semiconductor near the metal interface and concentrates carrier generation closed to the collection pathway. This localized excitation, coupled with drift-induced carrier separation and shortened diffusion length, can suppress recombination and improve charge extraction efficiency.[38,39,49]

To further increase the performance and value of products formed by solar water splitting devices, the oxygen evolution reaction (OER), which produces oxygen as a low-value byproduct, can be replaced with an oxidation reaction that produces high-value-added chemicals.[50] One of the most promising replacements is the glycerol oxidation reaction (GOR). As a byproduct of the biodiesel industry, glycerol is abundant and inexpensive. With an annual production exceeding 3–4 million tons and a market cost of approximately $0.11 per kg, glycerol is more economical than many alternative organic substrates.[51] The GOR (0.4 V_{RHE}) is thermodynamically more favourable than the OER (1.23 V_{RHE}), significantly reducing the photovoltage requirement for PEC devices,[52] thereby boosting H_2 production.[53] Also, glycerol oxidation can yield high-value chemicals such as dihydroxyacetone and glyceraldehyde, which hold much higher economic value than glycerol itself.[54,55] Among these products, dihydroxyacetone (DHA) is particularly valuable, and recent studies have demonstrated that BVO photoanodes can achieve selective oxidation of glycerol to DHA with high efficiency.[56] Also, PEC-driven routes have been shown to be more efficient and cost-effective than conventional methods such as microbial fermentation or thermal catalytic processes.[57,58]

In this work, we present a method for decorating fluorine-doped tin oxide (FTO) with plasmonic Pd NPs. On top of these Pd NPs, we then grow a BVO layer (BVO-coated Pd). Using UV-vis spectroscopy we demonstrated the plasmonic nature of these Pd NPs and using X-ray diffraction (XRD) and Raman spectroscopy we confirmed the crystal structures of Pd and BVO. The PEC performance of the modified samples showed that the presence of plasmonic Pd NPs significantly improved the onset potential and plateau photocurrent density in current–voltage (*J*–*V*) curves and quantum efficiency of light conversion in incident photon-to-current conversion efficiency (IPCE) measurements. TAS was also applied to study the charge carrier behaviour in the BVO-coated Pd samples, revealing unique absorption signals associated with plasmonic energy transfer. To further resolve the spectrally and temporally overlapping signals in TAS, we applied a model-free global analysis based on a genetic algorithm to extract distinct kinetic components. Overall, the improved performance of BVO-coated Pd provides a new strategy for enhancing the performance of PEC devices, with further insights into the mechanism of this enhancement revealed by time-resolved studies of their charge carrier behaviour.

2. Experimental section

2.1. Synthesis of bismuth vanadate (BVO) and Pd decoration by aerosol-assisted chemical vapor deposition (AACVD)

BVO films were fabricated in an aerosol-assisted chemical vapor deposition (AACVD) setup on FTO coated substrates (TEC 15, 2.5 × 1.3 cm, Pilkington NSG). The precursor solution was vanadium acetylacetonate ($V(acac)_3$, 0.073 g) and triphenyl bismuth ($Bi(Ph)_3$, 0.088 g) dissolved in a mixture of acetone and methanol (40 ml, 3 : 1). This solution was aerosolized using a humidifier (Liqui-fog®, Johnson Matthey, ~1.6 MHz operating frequency) and then carried into the reactor by air at a flow rate of 5 L min^{-1}. The aerosol was directed over the heated FTO substrate surface at 400 °C, leading to the deposition of BVO films. The films were later annealed in a muffle furnace (Nabertherm, L-092K1RN1) in air at 500 °C for 2 hours.

The BVO-coated Pd samples were prepared with a similar process. The Pd NPs are deposited on FTO with a precursor solution of palladium acetylacetonate ($Pd(acac)_2$, *X* mg, *X* = 1, 2, 4, 8, 12, 20) dissolved in 25 mL of methanol carried by N_2 at a flow rate of 2 L min^{-1}. The samples were cooled in N_2 atmosphere before the synthesis of BVO films *via* AACVD on its surface.

2.2. X-ray diffraction

X-ray diffraction (XRD) patterns were obtained using a Bruker D2 Phaser diffractometer featuring a PSD Linx Eye silicon strip

detector. The X-rays were generated with Cu $K_{\alpha1}$ radiation (λ = 1.54056 Å) and Cu $K_{\alpha2}$ radiation (λ = 1.54439 Å) at an intensity ratio of 2 : 1. Measurements were conducted on all samples over a 2θ range of 15° to 70°, with an angular increment of 0.03° and 1 s per step. The crystallite sizes were estimated using the Debye–Scherrer equation:[59]

$$D = \frac{K\lambda}{\beta\cos\theta} \quad (1)$$

where D is the average diameter of the Pd particles, K is the shape factor (set to 0.9),[51] λ is the X-ray wavelength (1.54056 Å for Cu $K\alpha_1$ radiation), β is the full width at half maximum observed (FWHM), and θ is the Bragg angle.

2.3. UV-vis

Transmittance and total reflectance spectra were measured using a SHIMADZU UV-vis spectrometer (UV-2600) with integrating sphere. The data was collected over the wavelength range of 400 nm to 700 nm with resolution of 0.1 nm. Absorptance spectra were calculated by subtracting the transmittance and total reflectance from unity.

2.4. Photoelectrochemical measurements

All photoelectrochemical measurements were conducted under a three-electrode system with a cappuccino cell[60] using an Autolab potentiostat (PGSTAT101, Metrohm). The three-electrode system consisted of Pt mesh counter electrode as the cathode, an Ag/AgCl saturated KCl reference electrode and the working electrode as the anode. All measurements were carried out from the BVO side (front illumination) with an electrolyte of 0.5 M Na_2SO_4 and 0.1 M K_2HPO_4/KH_2PO_4 buffer (pH = 7). The actual applied voltage was reported against the reversible hydrogen electrode (V_{RHE}), obtained with the Nernst equation:

$$V_{RHE} = V_{Ag/AgCl} + E^{\circ}_{Ag/AgCl} + 0.0591 \times pH. \quad (2)$$

In this equation, $V_{Ag/Agcl}$ is the applied potential against Ag/AgCl reference electrode, while $E^{\circ}_{Ag/AgCl}$ is the reference electrode standard potential.

Linear scan voltammetry (LSV) was utilized to measure the performance of our photoanodes in the light and dark across a range of applied voltages (with a scan rate of 25 mV s^{-1}). Chronoamperometry was utilised the measure the performance of our photoanodes in the light and dark at a fixed applied potential. All measurements were conducted under 1 sun simulated (white light) illumination provided by a 75 W Xenon lamp (Hamamatsu) with a KG3 filter.

IPCE was used to characterize the photocatalyst efficiency in converting photons to current under monochromatic light from 250–600 nm (produced by the same 75 W Xenon lamp with a monochromator) (OBB-2001, Photon Technology International). The intensity of the monochromatic light was measured by an optical power meter (PM100D, Thorlabs) with a power sensor (S120UV, Thorlabs). Chronoamperometry (CA) is used to apply a constant potential and measure current over time under different wavelength of monochromatic light and was also used to evaluate the stability and performance of photocatalysts in water splitting under equilibrium. The IPCE was calculated using the equation:

$$IPCE = \frac{1239 I_{ph}}{P_{mono}\lambda} \times 100\% \quad (3)$$

In this equation, I_{ph} (mA cm^{-2}) is the photogenerated current density. P_{mono} (mW cm^{-2}) and λ (nm) is the measured power and wavelength of the monochromatic light. 1239 is a constant derived from Planck's constant, the speed of light, and the electronvolt conversion factor, used to relate photon energy to wavelength in nanometres.

2.5. Scanning electron microscopy (SEM)

A SEM system (Zeiss Gemini Sigma300 FEG) in secondary electron mode is used to image the samples using an electron beam accelerating voltage of 5 kV and a working distance of ~5 mm. Signals of Energy Dispersive X-ray spectroscopy are shown with 10 points Savitzky–Golay smoothing on elemental signals.

2.6. Raman spectroscopy measurements

Raman spectroscopy measurements were taken with a Horiba LabRAM HR Evolution microscope at room temperature with a 532 nm green laser operating at 10% laser power, within 50 to 1000 cm^{-1} wavenumbers and a resolution of 0.52 cm^{-1}.

2.7. Transient absorption spectroscopy (TAS) and global analysis (GA)

The ultrafast transient absorption system uses a regeneratively amplified Ti:sapphire laser (Solstice, Spectra-Physics) to produce 800 nm laser pulses with a width of 92 fs at 1 kHz repetition rate. After the Solstice amplifier, pulses are split into pump and probe pulses. The pump pulse is tuned for wavelengths from ~290 nm to NIR using an optical parametric amplifier and a frequency mixer. The probe pulse is delayed by up to ~6 ns using a delay stage and then transformed into a white light continuum by focusing it through a sapphire crystal. This continuum covers a broad wavelength range and is split into two: one for probing the sample and the other for reference. Both are analysed using separate multichannel spectrometers. ΔA between the excited and ground states are measured by blocking alternate pump pulses with a rotating optical chopper. In this TAS measurement, BVO films and BVO-coated Pd samples are excited by a 400 nm pump when a delay probe is used to measure the ΔA in a visible continuum (450–700 nm) within the timescale from ~100 fs to ~6 ns. All tests are done under front illumination.

Furthermore, global analysis (GA) was utilized to combine data from different time points to fit models, helping to understand how dynamic processes evolve over time. In mathematics, global analysis, also known as analysis on manifolds, focuses on the global and topological characteristics of differential equations defined on manifolds and vector bundles. It employs methods from infinite-dimensional manifold theory

and the topology of mappings to classify the behaviour of differential equations, especially nonlinear ones. Global analysis of TAS data simultaneously fits a model to data from multiple time-resolved spectra to reveal separate dynamic processes. This approach enhances parameter accuracy by integrating data across different delay times and experimental conditions. It provides a holistic view of carrier dynamics and other transient phenomena, offering deeper insights than isolated analyses. MATLAB (R2020b) software was used to conduct global analysis for TAS measurements with a two-compartment model.

3. Results and discussion

In Fig. 1a, the XRD pattern collected from Pd-decorated glass (8 mg precursor) reveals a peak at 2θ = 40.1° and 46.8°, assigned to the (111) and (200) plane of face-centred cubic Pd (ICSD PDF #46-1043, space group $Fm\bar{3}m$, $a = b = c$ = 3.89 Å), confirming crystalline Pd growth. The diffraction patterns in Fig. 1b confirm the formation of the monoclinic BVO phase (ICSD PDF #48-0744) in all BVO-containing samples, with peaks from the underlying FTO substrate also observed (ICSD PDF # 99-000-0607). Sharper and more intense peaks are observed in the sample coated on Pd, indicating improved crystallinity of the BVO layer promoted by the Pd nanoparticles that reside underneath. The annealing step at 500 °C also improves the crystallinity of BVO, as evidenced by the sharper diffraction peaks in the XRD patterns (Fig. S1), while the FTO substrate remains unchanged. This treatment enhances the structural quality of the photoanode, further contributing to the improved PEC performance we observe. The crystallite sizes were estimated using the Debye–Scherrer equation (eqn (1)),[59] with sizes from select peaks of the Pd and BVO phases summarized in Table 1.

While Pd crystallites are ~30 nm in size, the BVO crystallites range from ~82.4 to 97.4 nm. A notable increase in BVO crystallite size is observed upon Pd loading (from 98.3 to 122.6 nm), suggesting a Pd-induced enhancement in crystal growth. These values represent lower bounds, as they do not account for structural defects or particle agglomeration seen in SEM images (Fig. 2).

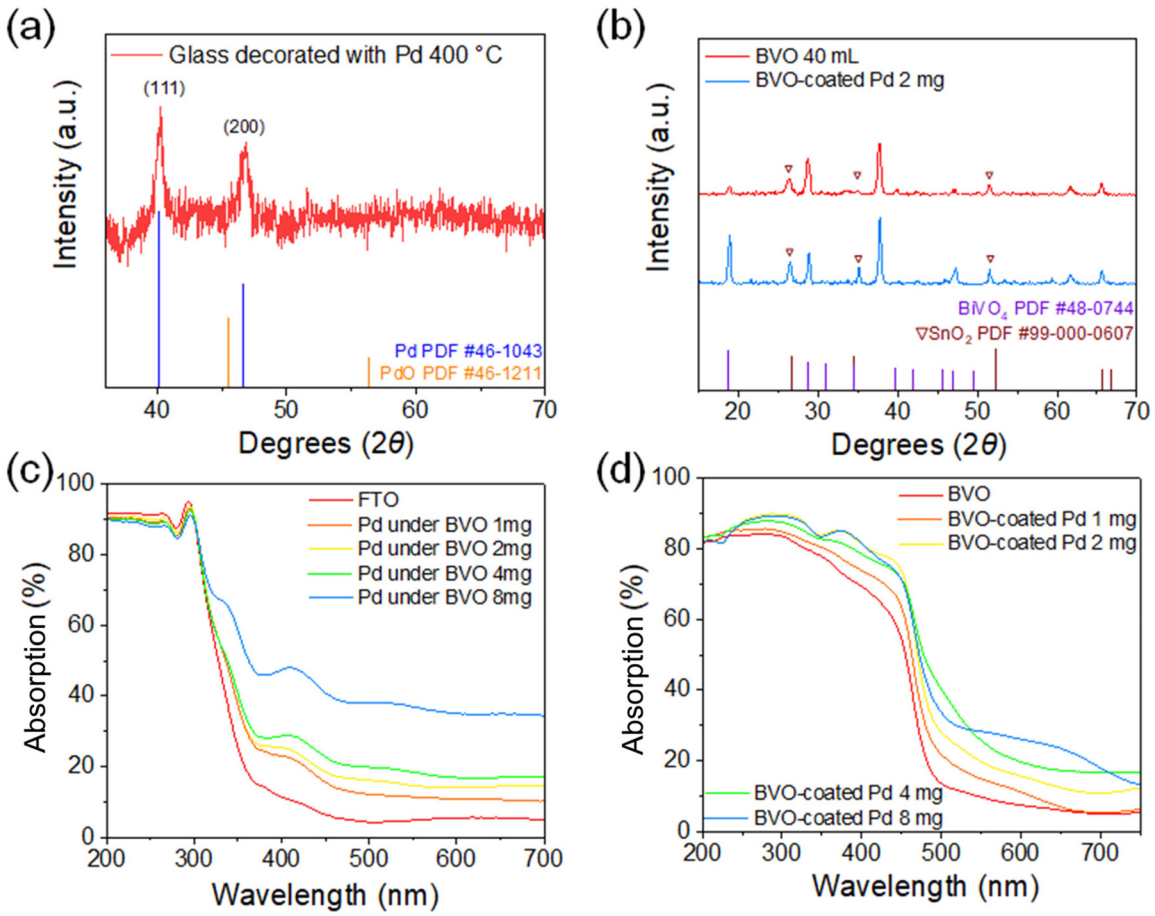

Fig. 1 (a) XRD pattern of glass decorated with Pd from 8 mg precursor, standard Pd data obtained from the ICSD PDF #46-1043, and standard PdO data obtained from the ICSD PDF #46-1211. (b) XRD patterns of BVO, BVO-coated Pd from 2 mg precursor, standard BVO data obtained from the ICSD PDF #48-0744 and standard SnO_2 data (i.e. FTO) obtained from the ICSD PDF #48-0744. (c) Absorptance spectra of Pd-coated FTO samples and FTO. (d) Average absorptance spectra of BVO and BVO-coated Pd sample, with three distinct samples used to produce the average.

Table 1 Crystallite sizes (D) of Pd and BVO samples calculated using the Debye–Scherrer equation from selected XRD peaks

	Peak position 2θ (°)	Peak assignment	FWHM β (rad)	Crystal size D (nm)
Pd on FTO 8 mg	40.1	Pd (111)	0.063	28.8
	46.8	Pd (200)	0.052	39.8
BVO 40 ml	18.9	BVO (101)	0.017	85.9
	28.8	BVO (112)	0.019	82.4
	37.7	BVO (114)	0.018	97.4
BVO-coated Pd 2 mg	18.9	BVO (101)	0.015	98.3
	28.9	BVO (112)	0.013	122.6
	37.8	BVO (114)	0.015	114.3

Optical absorption measurements in Fig. 1c show that Pd-coated FTO substrates exhibit markedly higher absorptance than bare FTO. The broad spectral response of these samples is consistent with a broadband plasmonic effect, attributed to the size and shape variation of the Pd nanoparticles.[61,62] Fig. 1d presents the averaged absorptance spectra of BVO and Pd-coated BVO samples with varying Pd precursor amounts. All Pd-containing samples display enhanced absorption from 250 nm to 700 nm, likely resulting from LSPR and surface plasmon polariton effects introduced by the Pd–semiconductor interface.[26,63] Fig. S2 shows the average absorptance spectra with one standard deviation error and Fig. S3 shows the transmittance and reflectance spectra of all samples.

As further shown in Fig. S4a and b, the Raman spectra confirmed the characteristic peaks of monoclinic BVO, which remained unchanged with small Pd loadings beneath the BVO layer, while heavy Pd deposition disrupted BVO crystallinity.[64] A weak feature around 650 cm^{-1} was observed for the 2 mg Pd sample, likely originating from the FTO substrate and enhanced through a surface-enhanced Raman scattering effect, which could further attest the plasmonic behavior of Pd on FTO.[65]

The fabrication process of BVO-coated (*i.e.* BVO-coated) Pd electrodes is illustrated in Fig. 2a. Pd nanoparticles were first deposited on FTO substrates using an AACVD process. The aerosol of $Pd(acac)_2$ dissolved in methanol was carried using nitrogen gas into a reactor held at 400 °C, where the thermal decomposition of the precursor resulted in Pd NP formation. This was followed by the AACVD deposition of a BVO layer from the aerosol of $Bi(Ph)_3$ and $V(acac)_3$ dissolved in an acetone: methanol mixture carried using air into a reactor held at 400 °C. By varying the Pd precursor transferred (2–8 mg), different surface coverages were achieved (Fig. S5).

Top-down scanning electron microscopy (SEM) images reveal the evolution of surface morphology with increasing Pd precursor. The pristine FTO surface (Fig. 2b) is composed of densely packed, polycrystalline grains with irregular shapes and sharp boundaries.[66] This texture is characteristic of FTO and beneficial for light scattering and film adhesion. Upon deposition using 2 mg Pd precursor (Fig. 2c), uniformly distributed Pd nanoparticles with diameters around 5 nm appear on the FTO surface. At 4 mg of precursor transfer (Fig. 2d), the density of Pd increases, and particles begin to cluster with sizes around 10 nm. Further increasing the precursor transfer to 8 mg (Fig. 2e) leads to extensive surface coverage by Pd nanoparticles, some of which grow to ~30 nm, along with a background population of smaller clusters. Top-down SEM images of an exemplar BVO-coated 8 mg sample is shown in Fig. S6, with the BVO layer seen to completely cover the Pd particles beneath, forming globular structures around 200 nm in diameter.

Cross-sectional analyses of the BVO-coated Pd sample are shown in Fig. 2f and g. A line scan energy-dispersive X-ray spectroscopy (EDS) across the vertical interface confirms the presence and distribution of Si, Bi, Pd, Sn, and V elements. The BVO layer is ~200 nm thick and lies on a ~500 nm FTO substrate. The clear signal of the Pd layer embedded beneath BVO further indicates good integration between the metal and semiconductor. The BVO layer also acts as a protective layer, preventing Pd from being oxidized to PdO under an applied positive voltage, as shown in the Pourbaix diagram in Fig. S7. With increasing Pd loading, the overall nanoparticle coverage increases, which can enhance the plasmonic effect and light absorption. However, excessive Pd may compromise the photoelectrochemical performance of the photoanode due to two factors. Firstly, strong plasmonic coupling between neighbouring Pd particles can dampen the LSPR, reducing its beneficial optical effects.[67,68] Secondly, a higher density of Pd may introduce energy level misalignment at the metal–semiconductor interface, potentially forming a Schottky barrier that hinders efficient charge transfer and promotes carrier accumulation. Control over nanoparticle loading is therefore critical. While moderate Pd incorporation promotes light absorption and charge separation, excessive aggregation may diminish the overall photoelectrochemical activity.

PEC measurements were conducted to evaluate the effect of Pd NPs incorporation on the performance of the BVO photoanodes. As shown in the linear sweep voltammetry (LSV) curves under front-side illumination (Fig. 3a), all BVO-coated Pd samples display improved photocurrent densities compared to pristine BVO. Among them, the BVO-coated Pd 4 mg sample achieves the highest current density of 0.85 mA cm^{-2} at 1.23 V_{RHE}, corresponding to a 36% improvement relative to bare BVO. Upon introducing 0.5 M glycerol as a hole scavenger (Fig. 3b), the photocurrent of BVO-coated Pd 4 mg further increases to 1.58 mA cm^{-2} at the same potential. This represents a 32% enhancement compared to BVO with glycerol, and a total increase of 158% when compared to bare BVO without glycerol. These results highlight the synergistic role of Pd and glycerol in promoting charge separation and suppressing recombination. JV curves for a range of glycerol concentrations (0.1 to 1.5 M) are shown for both the bare BVO and BVO-coated Pd 4 mg samples in Fig. S8, where optimal activity was seen at 0.5 M glycerol in both cases.

The stability of the photoanodes was examined using chopped light chronoamperometry, as shown in Fig. 3c and d. In the absence of glycerol (Fig. 3c), the bare BVO electrode exhibited a rapid decay in photocurrent over time, which is

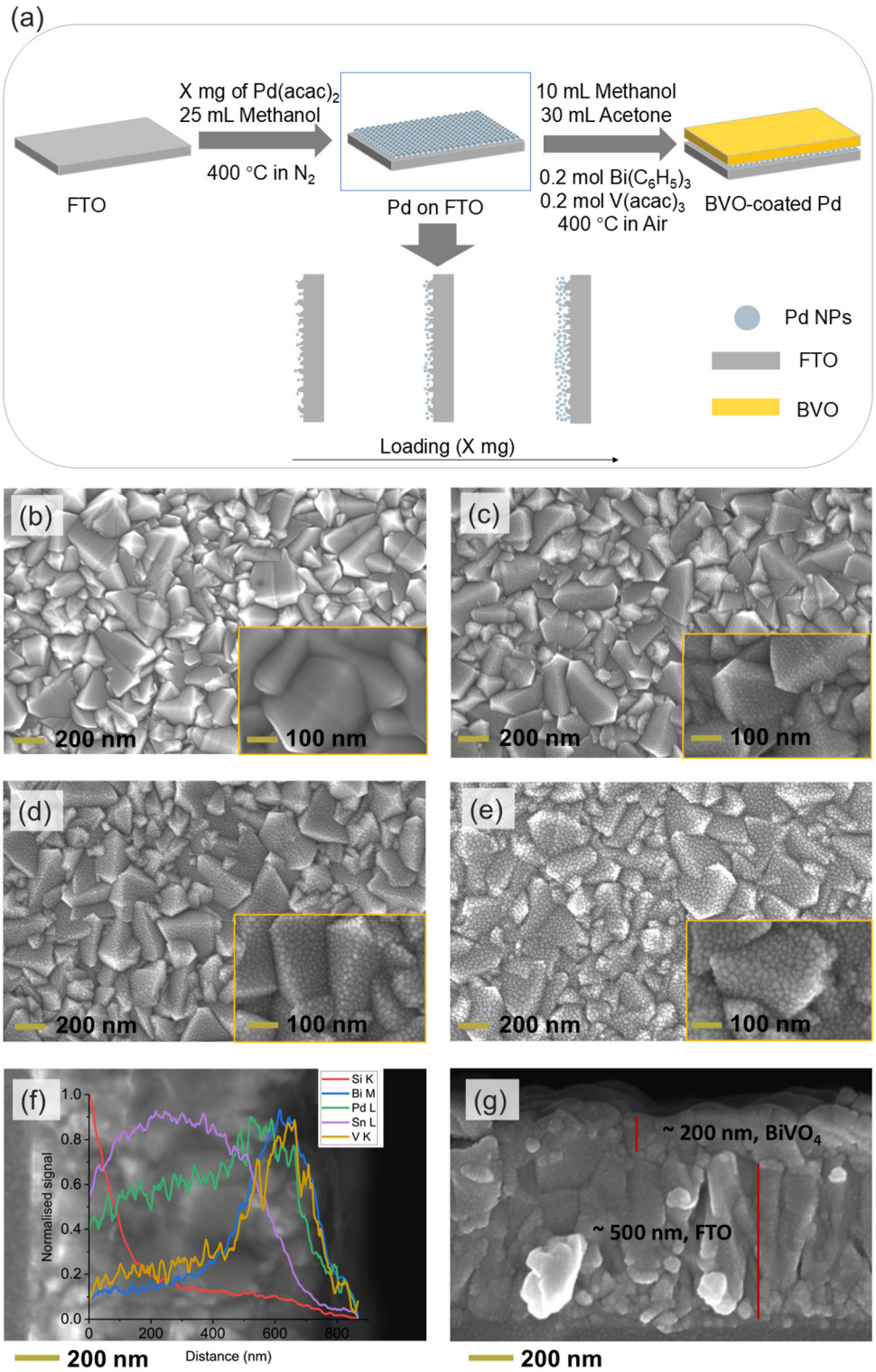

Fig. 2 (a) Schematic of our fabrication process of BVO-coated Pd and the surface decoration of FTO. Top-down SEM images of (b) FTO, (c) glass decorated with Pd from 2 mg precursor, (d) glass decorated with Pd from 4 mg precursor, (e) glass decorated with Pd from 8 mg precursor. The main images are measured at a magnification of 100k while the insets are measured at a magnification of 400k. (f) Linear scan energy dispersive X-ray spectroscopy of BVO-coated Pd 8 mg. (g) A side-on view of BVO-coated Pd 8 mg showing the approximate thicknesses of the BVO layer (~200 nm) and FTO substrate (~500 nm) taken at a magnification of 100k. All SEM images are measured with 5 keV electron beam power.

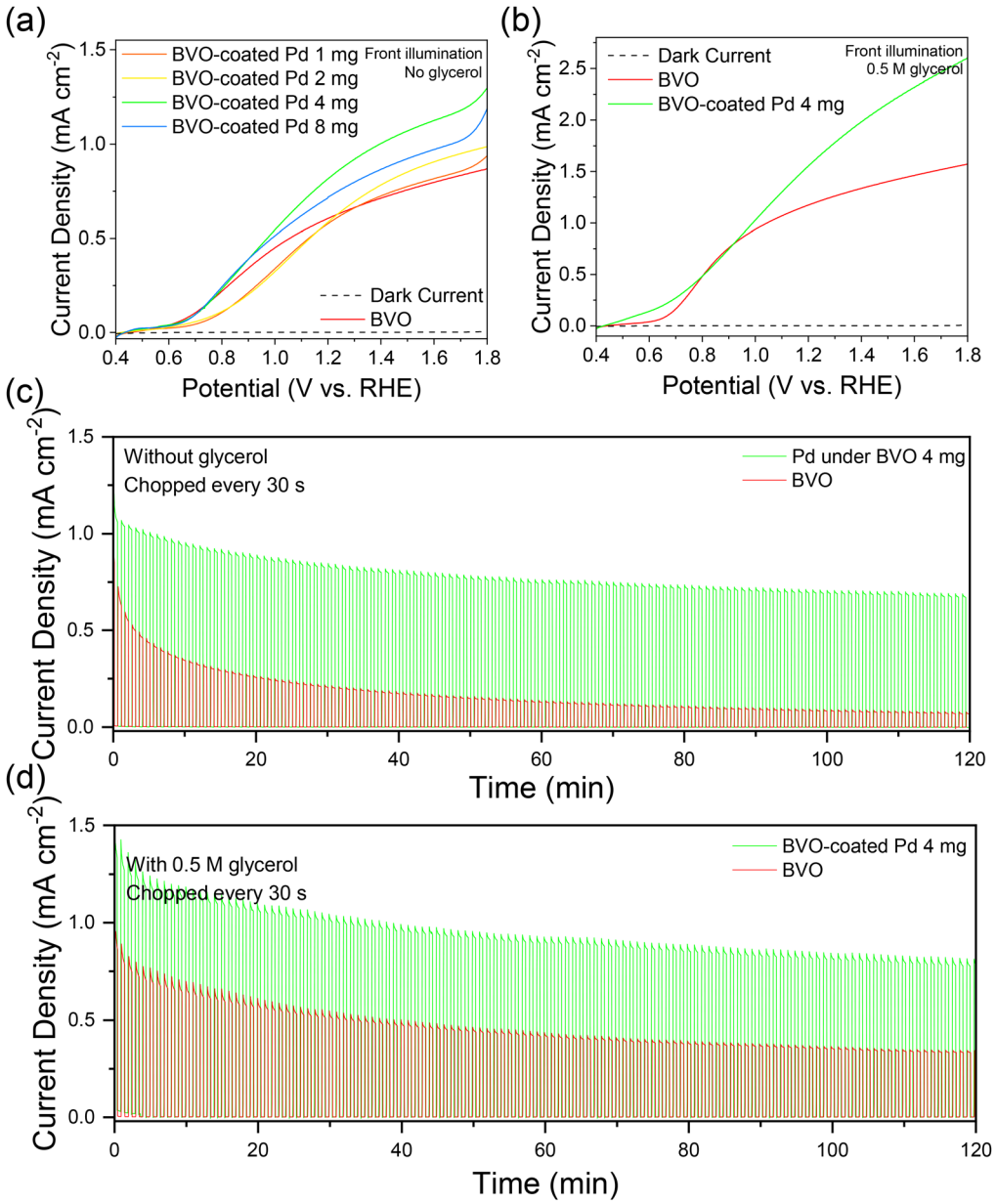

Fig. 3 (a) Forward scanning LSV measurements of BVO-coated Pd and BVO photoanodes. (b) LSV measurement of BVO-coated Pd from 4 mg precursor and BVO photoanodes with an addition of 0.5 M glycerol. Chopped photocurrent density-time profiles of BVO and BVO-coated Pd photoanodes at an applied voltage of 1.23 V_{RHE} (c) without addition of glycerol and (d) with an addition of 0.5 M glycerol. An automatic chopper is used to modulate light on/off with a frequency of 30s. Conditions: front illumination, electrolyte 0.5 M Na_2SO_4 (aq) + 0.1 M K_2HPO_4/KH_2PO_4, pH 7, under illumination with a 75 W Xe lamp with a KG3 filter set to match the intensity, 100 mW cm^{-2} of 1 sun condition, Scan rate: 25 mV s^{-1}.

commonly attributed to surface recombination and the accumulation of oxygen or oxidation byproducts.[69] In contrast, BVO-coated Pd 4 mg maintained a higher initial photocurrent and exhibited significantly improved stability, retaining 58.1% of its initial value after 2 hours, whereas bare BVO retained only 10.6%.[70] In the presence of 0.5 M glycerol (Fig. 3d), both BVO and BVO-coated Pd 4 mg showed enhanced photocurrent retention due to the suppression of competitive water oxidation and side reactions.[71,72] Nonetheless, BVO-coated Pd 4 mg continued to outperform bare BVO, with 49.5% retention compared to 36.3% after 2 hours, suggesting that the Pd nanoparticles provide additional functional benefits beyond the effect of the hole scavenger alone. ^{1}H NMR measurements of aliquots from bare BVO samples indicated that the oxidation products of glycerol were dihydroxyacetone (DHA) and formic acid (FA), in an approximate ratio of 1 : 2 (Fig. S9). Control experiments confirmed that Pd nanoparticles alone are unstable under bias. As shown in Fig. S10, Pd/FTO exhibited a high initial current that rapidly decayed in successive scans, with CV curves indicating Pd redox transitions consistent with

its thermodynamic instability. Similarly, Pd deposited on top of BVO also showed a progressive photocurrent loss upon repeated scans (Fig. S11), highlighting the BVO-coated Pd structure preserve its plasmonic contribution in PEC applications.

The overall improvement in PEC performance can be attributed to multiple roles by the Pd NPs. The LSPR effect of Pd enhances visible light absorption, while the formation of a Schottky junction at the Pd/BVO interface facilitates charge separation, preventing charge recombination at the surface.[26] Furthermore, Pd sites may provide additional transfer route, which act as temporary sinks for photogenerated electrons, reducing surface recombination and delaying product accumulation. These effects collectively contribute to both improved initial photocurrent and enhanced long-term stability.

IPCE measurements were performed at 1.23 V_{RHE} to further evaluate the photo response of the photoanodes under monochromatic illumination. Fig. 4a shows the IPCE spectra of BVO with varying concentrations of glycerol. A gradual increase in IPCE is observed as the glycerol concentration is increased from 0.1 M to 0.5 M, after which the enhancement plateaus. This trend suggests that at 0.5 M glycerol a mass transfer limit is reached, where further additions of glycerol does not result in further improvements in hole carrier extraction. A similar behaviour is observed for the BVO-coated Pd 4 mg sample (Fig. 4b), where the IPCE also peaks at 0.5 M glycerol, confirming that glycerol benefits this system by facilitating more efficient charge separation. Additional IPCE spectra at 1.23 V_{RHE} for a range of BVO-coated Pd samples (1, 2 and 8 mg) at a range of glycerol concentrations (0.1 to 1.5 M) are shown in Fig. S12, with optimal activity seen at 0.5 M.

Direct comparison of IPCE spectra with and without glycerol addition is shown in Fig. 4c and d. In the presence of 0.5 M glycerol, the IPCE of BVO increases by approximately 10% across the measured wavelength range, whereas the BVO-coated Pd 4 mg sample exhibits a more substantial improvement of around 20%. The maximum IPCE of BVO-coated Pd reaches above 45% under these conditions, significantly exceeding that of bare BVO without glycerol, which remains around 15%. These results underscore the superior light-harvesting and interfacial charge transfer properties of the BVO-coated Pd photoanode.

The enhancement in IPCE can be attributed to the combined effects of glycerol oxidation and Pd plasmonic behaviour. Glycerol acts as a sacrificial hole donor, driving the GOR, which is more thermodynamically favourable than the OER.[73] This reaction significantly boosts IPCE as glycerol oxidation reduces charge-transfer resistance,[74] with IPCEs of ~55% seen in glycerol-enhanced PEC systems.[72] Meanwhile, the presence of Pd NPs contributes through LSPR, extending the range of

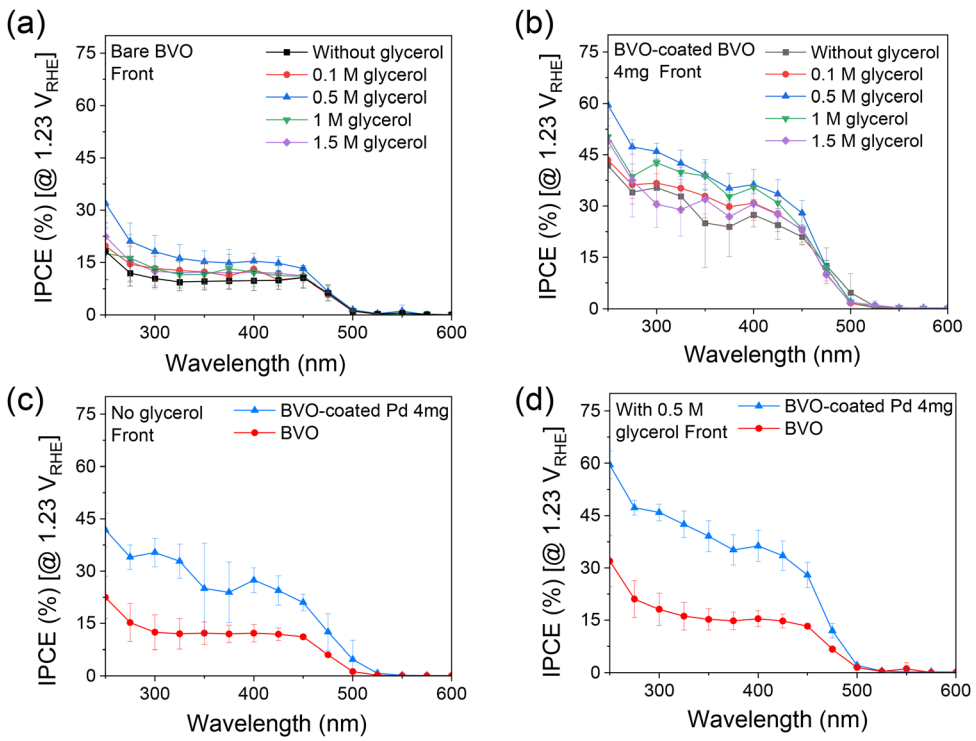

Fig. 4 (a) IPCE spectra of BVO with and without the addition of 0.1, 0.5, 1.0 and 1.5 M glycerol, measured at 1.23 V_{RHE}. (b) IPCE spectra of BVO-coated Pd from 4 mg precursor with and without the addition of 0.1, 0.5, 1 and 1.5 M glycerol, measured at 1.23 V_{RHE}. (c) IPCE spectra of BVO-coated Pd from 4 mg precursor and BVO without the addition of glycerol measured at 1.23 V_{RHE}. (d) IPCE spectra of BVO-coated Pd from 4 mg precursor and BVO with the addition of 0.5 M glycerol, measured at 1.23 V_{RHE}. All IPCE spectra are produced with data from three samples, with uncertainty bars of each data point calculated with a standard deviation of 1σ shown. Conditions: front illumination, electrolyte 0.5 M Na_2SO_4 (aq) + 0.1 M K_2HPO_4/KH_2PO_4, pH 7, under illumination by a 75 W Xe lamp with a KG3 filter, set to match the intensity of 100 mW cm^{-2} for 1 sun intensity.

light absorption and providing additional excitation and electron-transfer pathways, which reduce bulk and surface recombination losses. The synergy between enhanced hole extraction by glycerol and improved electron dynamics *via* Pd plasmonic effects leads to a marked increase in the photoanode's external quantum efficiency and PEC activity.

Transient absorption spectroscopy (TAS) was further performed to investigate the ultrafast charge carrier dynamics in BVO and Pd-modified BVO photoelectrodes. In TAS, positive ΔA signals are primarily attributed to excited-state absorption (ESA), or the absorption by photogenerated intermediate species, whereas negative ΔA signals typically arise from ground-state bleaching (GSB) or stimulated emission.[75,76] In the case of BVO, the dominant contributors to the positive transient signals are generally associated with ESA from photogenerated electrons and absorption features related to hole trapping.[77–80] In the sub-500 nm region, especially near 470 nm, the signal is primarily attributed to ESA by electrons.[79] In contrast, the absorption above 500 nm is dominated by hole-related processes, particularly transitions involving trapped holes at or near the surface. While earlier interpretations generally assigned the 470 nm peak to photogenerated hole absorption, more recent experimental and modelling studies suggest that ESA by conduction band electrons and electron polarons is the predominant mechanism in this range.[78,80] Therefore, both spectral position and time dynamics must be considered to accurately identify the contributing charge carrier species. Power dependence TA (0.4 to 1.4 μJ per pulse) for both BVO and BVO-coated Pd 4 mg in an N_2 environment are shown in Fig. S13a. To exclude the possible influence of O_2 in the air, a comparison of the TA measured in an N_2 environment for BVO and BVO-coated Pd samples with 2 and 4 mg of precursor are shown in Fig. S13b, which indicates similar results to those seen in air in Fig. 5.

Fig. 5a and b compare the TA spectral evolution of pristine BVO and BVO-coated Pd 4 mg samples from 100 fs to 5000 ps under 400 nm pump excitation. Both samples exhibit a prominent positive ΔA feature centred near 470 nm, corresponding to excited-state absorption of photogenerated electrons.[81] The BVO-coated Pd samples show a higher amplitude and broader response extending into the near-infrared (NIR) region, indicating more efficient electron generation due to plasmon-enhanced excitation. The broad NIR signal is characteristic of LSPR in Pd nanoparticles,[82] where it was previously suggested that hot electrons of the plasmon may be injected into the semiconductor conduction band or shallow trap states.[41,83]

In the BVO-coated Pd samples, the early-time (<~1 ps) the positive TA signals in the >500 nm region (denoted as Region C in Fig. 5b) increase in intensity as Pd loading increases (Fig. 5c). This enhancement suggests that Pd incorporation introduces plasmonic-coupled states participating and facilitating charge separation. The respective electron transfer channels have transient character that reduces the probability of direct electron–hole recombination, effectively prolonging charge carrier lifetime.[78,84]

In addition, BVO-coated Pd from 4 mg precursor shows a significantly stronger TA signal in the sub-470 nm region (Region B in Fig. 5b) compared to pristine BVO. This spectral

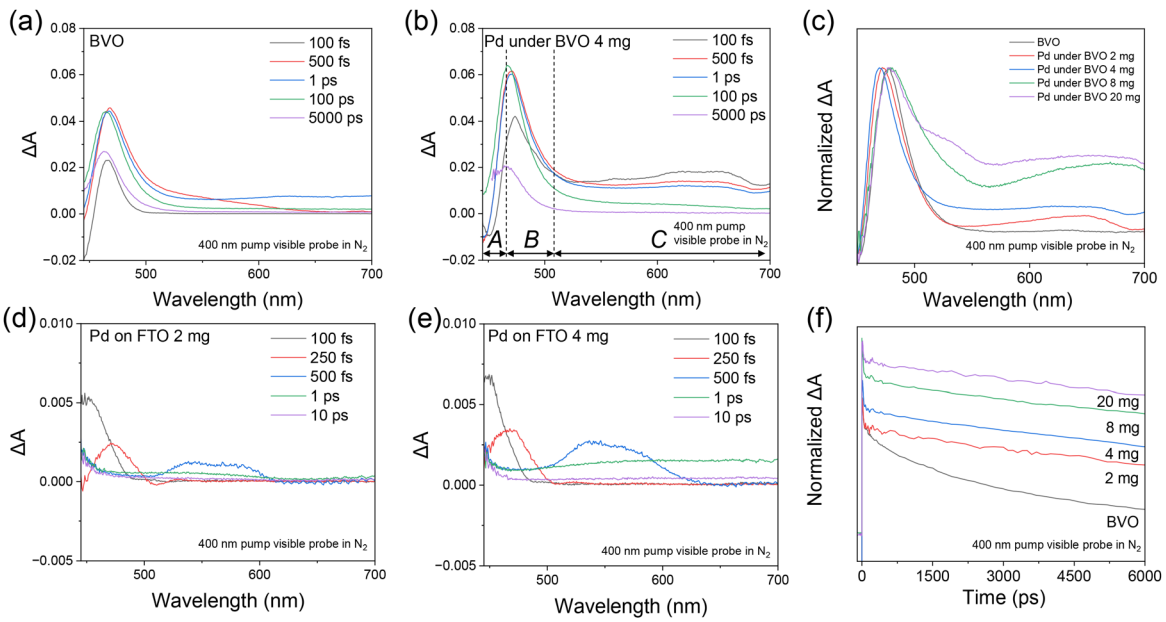

Fig. 5 Transient absorption spectra from 100 fs to 6000 ps after the pump for: (a) BVO and (b) BVO-coated Pd from 4 mg precursor. (c) Transient absorption spectra and kinetics of BVO and BVO-coated Pd with deposition precursors of 2, 4, 8, & 20 mg measured with 1 μJ 400 nm pump and visible probe in a time scale of 1 ps. (d) Pd on FTO from 2 mg precursor. (e) Pd on FTO from 4 mg precursor. All measurements were conducted with a 400 nm pump with power of 1.04 μJ and visible probe in an N_2 atmosphere. (f) Comparison between the TAS decay signals in BVO and BVO-coated Pd from 2, 4, 8 mg precursor samples at the probe wavelength of 480 nm.

range is generally attributed to ESA by conduction band electrons or electron polarons. The increased signal in this region points to a higher density of excited electrons, which is consistent with hot electron injection from Pd into the BVO conduction band. This observation further supports the existence of a plasmon-induced or catalytically facilitated hot electron transfer process, which elevates the early-time electron population in the TAS measurement window.

Fig. 5c demonstrates the influence of Pd loading on the transient spectra. As the amount of Pd precursor increases from 2 to 20 mg, the NIR transient absorption amplitude becomes progressively stronger. This observation is consistent with enhanced LSPR excitation and the generation of a greater number of hot carriers.[26,85] These carriers be can either directly injected into the BVO layer or transfer energy through near-field coupling, improving charge separation and delaying recombination. Notably, the BVO-coated Pd 20 mg sample exhibits the strongest TA response, suggesting maximum plasmonic enhancement at the highest loading level.

Fig. 5d and e show the transient spectra of Pd on FTO samples from 2 and 4 mg precursor, respectively. Short-lived features within the first few hundred femtoseconds are observed, consistent with surface plasmon polariton (SPP) excitation and subsequent hot carrier generation. The signals decay rapidly, indicating fast thermalization and limited charge retention in the absence of a semiconductor interface.

To assess electron dynamics, TAS decay profiles at a probe wavelength of 480 nm are compared in Fig. 5f. All Pd-coated samples exhibit longer-lived signals than pristine BVO, indicating suppressed recombination and enhanced charge stabilization. Fitting results summarised in Table 2 reveal that the second lifetime component (τ_2) of BVO is approximately 2.4 ns, while BVO-coated Pd samples show extended τ_2 values from ~7 to 10 ns. The BVO-coated Pd 20 mg sample shows a particularly long τ_1 and τ_2, indicating significant suppression of charge recombination. This trend suggests that photogenerated electrons can transfer to the Pd NPs introduced plasmonic-coupled states, thereby reducing the direct recombination within the BVO.[84,86,87] However, excessively high Pd loading may also introduce drawbacks. In the case of the 20 mg sample, the unusually long τ_2 could originate from the formation of deep interfacial trap states or reduced light penetration due to nanoparticle overaccumulation. Although this results in extended electron lifetime, it may also hinder light

Table 2 Fitting parameters of the TAS dataset collected with the BVO and BVO-coated Pd from 2, 4, 8 and 20 mg precursor electrodes

	BVO	BVO-coated Pd 2 mg	BVO-coated Pd 4 mg	BVO-coated Pd 8 mg	BVO-coated Pd 20 mg
τ_1 (ps)	16 ± 1	20 ± 1	23 ± 2	41 ± 3	59 ± 10
τ_2 (ps)	2400 ± 100	7800 ± 1000	8200 ± 2000	8500 ± 2000	9800 ± 2000
A_1	41%	42.60%	45.30%	43.90%	46.60%
A_2	58.90%	57.40%	54.70%	56.10%	54.40%

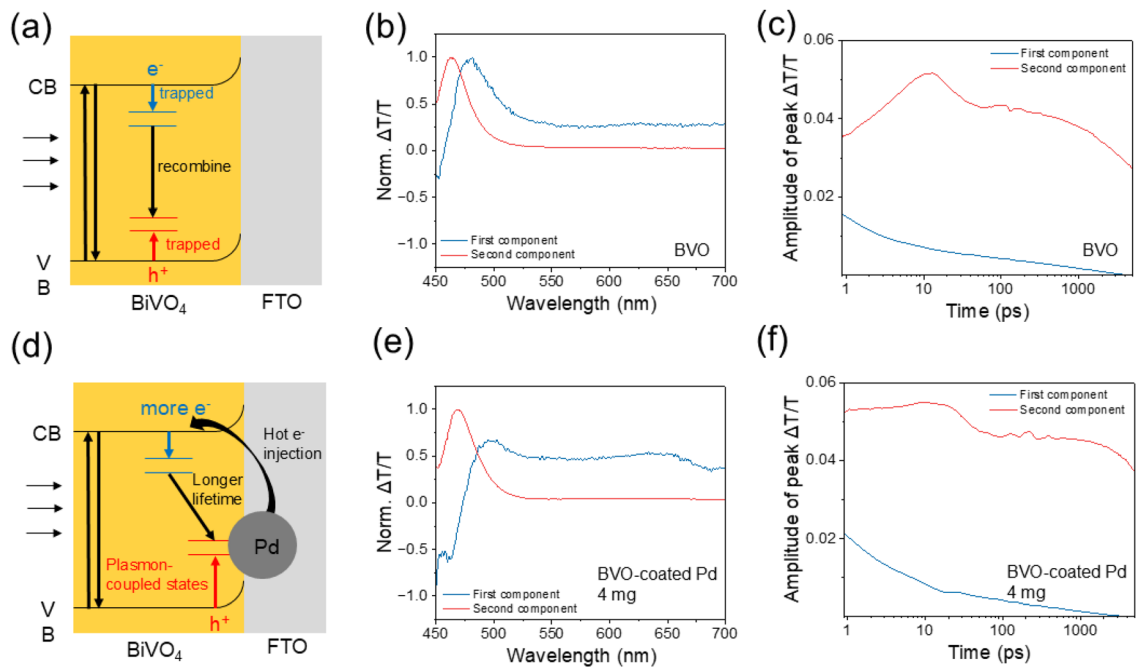

Fig. 6 Schematic of mechanisms of charge transport in (a) BVO and (d) BVO-coated Pd. Global analysis of simulated data from a two-compartment model: (b) the species associated spectra (SAS) and (c) decay traces of BVO. (e) SAS and (f) decay traces of BVO-coated Pd from 4 mg precursor.

from reaching the BVO layer, potentially limiting PEC performance.

To better resolve the overlapping spectral and temporal signatures in the transient absorption data, we applied a two-component global analysis based on a genetic algorithm. This model-free fitting approach separates the measured signal into two spectrally and kinetically distinct components, which are presented for two representative samples in Fig. 6. Panels (b) and (e) display the normalized spectra of the extracted components, while panels (c) and (f) show their corresponding decay traces across the probed time window. These plots allow direct identification of the contributing species and their temporal evolution.[47] The GA analyses for BVO-coated Pd 8 mg and BVO-coated Pd 20 mg are shown in Fig. S14, and the detailed methodology and description can be found in the SI (Fig. S15).

The schematic diagrams in Fig. 6a and d summarize the proposed photoinduced charge carrier dynamics in pristine BVO and BVO-coated Pd. In the pristine system (Fig. 6a), photogenerated electrons and holes are rapidly trapped within a few picoseconds and then recombine on the nanosecond timescale, limiting both carrier lifetime and photoelectrochemical efficiency. Upon Pd incorporation (Fig. 6d), two beneficial effects emerge: (i) the formation of plasmon-coupled states that extend hole lifetime, and (ii) the injection of hot electrons from Pd into the BVO conduction band, increasing the conduction electron population. Together, these processes suppress recombination and enhance the usable charge carrier density under illumination.[80,88]

The global analysis results shown in Fig. 6b, c, e and f provide further support for these interpretations. Two distinct spectrotemporal components were extracted from the datasets. The first component (blue line), dominant in the >470 nm region, corresponds to long-lived carriers and hole-related absorption, especially from trapped holes. Its amplitude is significantly higher in the Pd-modified sample (Fig. 6e) than in pristine BVO (Fig. 6b), consistent with the presence of additional plasmon-coupled states introduced by Pd. The second component (red line), dominant below 470 nm, is attributed to conduction band electrons or shallow traps. In the BVO-coated Pd sample, this component appears more intense within the first 10 ps (Fig. 6f), indicating a higher initial electron population. This behaviour is consistent with ultrafast hot electron injection from Pd nanoparticles into BVO. Taken together, these findings support the dual role of Pd in improving charge separation through both increased hole trapping and enhanced early-time electron injection.

4. Conclusions

In this study, we developed a synthetic route to BVO photoanodes decorated with plasmonic Pd nanoparticles using a novel AACVD method to improve the efficiency of solar-driven value-added glycerol oxidation. SEM, EDS, UV-vis, and XRD confirmed that the introduction of Pd nanoparticles enhanced visible light absorption through localized surface plasmon resonance and promoted higher BVO crystallinity, which benefits charge transport. Photoelectrochemical measurements showed that a moderate Pd loading (prepared with 4 mg of Pd precursor) significantly increased photocurrent density at 1.23 V_{RHE}, where the current rose from 0.62 mA cm^{-2} without glycerol (in bare BVO samples) to 1.58 mA cm^{-2} with glycerol (in BVO_4-coated Pd samples), as well as a boost of the IPCE from ~15% to ~40%. Stability was also improved, where under chopped light chronoamperometry for 2 hours without glycerol, the Pd coated BVO_4-coated Pd photoanode retained 58.1% of its initial photocurrent, whereas the bare BVO electrode only retained 10.6%. Transient absorption spectroscopy with global analysis revealed that Pd nanoparticles introduced additional pathways for charge carrier transfer. Hot electron injection from Pd into BVO increased conduction band electron density shortly after photoexcitation, while new plasmon-coupled states prolonged hole lifetime and reduced recombination. Together, these findings highlight the potential of integrating plasmonic nanoparticles with BVO photoanodes to improve solar water splitting and selective organic oxidation. We envisage that this strategy can be applied in related systems to improve the efficiency, stability, and economic viability of solar fuels and chemicals production.

Author contributions

J. X. and B. T. performed data curation, methodology, formal analysis, investigation and writing – original draft. Y. C. and L. L. assisted with data curation in carrying out transient absorption measurements. Z. L. and K. L. helped with methodology in sample preparation. A. K. and A. B. offered supervision, conceptualization, project administration and writing – review & editing.

Conflicts of interest

There are no conflicts of interest to declare.

Data availability

The data that support the findings of this study are available upon request.

Supplementary information is available, which includes additional data from XRD, UV-visible absorptance (including transmission and total reflectance), Raman spectroscopy, photographs and additional SEM images of our samples, a Pourbaix diagram of Pd, additional LSVs, CVs and IPCE, ^{1}H NMR data of production selectivity and TA data with details on our global analysis fitting. See DOI: **https://doi.org/10.1039/d5qi01542a**.

Acknowledgements

Y. C. and A. A. B. acknowledge support from UKRI/EPSRC (ActionSpec, Grant Ref: EP/X030822/1). K. L. thanks Imperial

College London for a Dean's PhD Scholarship. B. T. and A. K. thank the EPSRC for a Programme Grant (EP/W017075/1). L. L. acknowledges funding by the Imperial College London President's PhD Scholarships.

References

1 J. Hansen, M. Sato, R. Ruedy, K. Lo, D. W. Lea and M. Medina-Elizade, Global temperature change, *Proc. Natl. Acad. Sci. U. S. A.*, 2006, **103**(39), 14288–14293.
2 J. B. C. Jackson, Ecological extinction and evolution in the brave new ocean, *Proc. Natl. Acad. Sci. U. S. A.*, 2008, **105**, 11458–11465.
3 P. C. D. Milly, R. T. Wetherald, K. A. Dunne and T. L. Delworth, Increasing risk of great floods in a changing climate, *Nature*, 2002, **415**(6871), 514–517.
4 X. H. Lu, S. L. Xie, H. Yang, Y. X. Tong and H. B. Ji, Photoelectrochemical hydrogen production from biomass derivatives and water, *Chem. Soc. Rev.*, 2014, **43**(22), 7581–7593.
5 M. I. Hoffert, Farewell to Fossil Fuels?, *Science*, 2010, **329**(5997), 1292–1294.
6 L. Fulcheri and Y. Schwob, From methane to hydrogen, carbon black and water, *Int. J. Hydrogen Energy*, 1995, **20**(3), 197–202.
7 A. Fujishima and K. Honda, Electrochemical Photolysis of Water at a Semiconductor Electrode, *Nature*, 1972, **238**(5358), 37–38.
8 H. Song, S. Luo, H. Huang, B. Deng and J. Ye, Solar-Driven Hydrogen Production: Recent Advances, Challenges, and Future Perspectives, *ACS Energy Lett.*, 2022, **7**(3), 1043–1065.
9 A. Kudo, K. Omori and H. Kato, A Novel Aqueous Process for Preparation of Crystal Form-Controlled and Highly Crystalline $BiVO_4$ Powder from Layered Vanadates at Room Temperature and Its Photocatalytic and Photophysical Properties, *J. Am. Chem. Soc.*, 1999, **121**(49), 11459–11467.
10 S. Zhou, K. Chen, J. Huang, L. Wang, M. Zhang, B. Bai, H. Liu and Q. Wang, Preparation of heterometallic CoNi-MOFs-modified $BiVO_4$: a steady photoanode for improved performance in photoelectrochemical water splitting, *Appl. Catal., B*, 2020, **266**, 118513.
11 F. F. Abdi, L. Han, A. H. Smets, M. Zeman, B. Dam and R. Van De Krol, Efficient solar water splitting by enhanced charge separation in a bismuth vanadate-silicon tandem photoelectrode, *Nat. Commun.*, 2013, **4**(1), 2195.
12 B. Tam, S. D. Pike, J. Nelson and A. Kafizas, The scalable growth of high-performance nanostructured heterojunction photoanodes for applications in tandem photoelectrochemical-photovoltaic solar water splitting devices, *Chem. Sci.*, 2025, **16**, 7794–7810.
13 V. Andrei, R. A. Jagt, M. Rahaman, L. Lari, V. K. Lazarov, J. L. MacManus-Driscoll, R. L. Hoye and E. Reisner, Long-term solar water and CO_2 splitting with photoelectrochemical BiOI–$BiVO_4$ tandems, *Nat. Mater.*, 2022, **21**(8), 864–868.
14 X. Chang, T. Wang, P. Zhang, J. Zhang, A. Li and J. Gong, Enhanced Surface Reaction Kinetics and Charge Separation of p–n Heterojunction Co_3O_4/$BiVO_4$ Photoanodes, *J. Am. Chem. Soc.*, 2015, **137**(26), 8356–8359.
15 M. Liu, Y. Chen, J. Su, J. Shi, X. Wang and L. Guo, Photocatalytic hydrogen production using twinned nanocrystals and an unanchored NiS_x co-catalyst, *Nat. Energy*, 2016, **1**(11), 1–8.
16 A. Kudo and Y. Miseki, Heterogeneous photocatalyst materials for water splitting, *Chem. Soc. Rev.*, 2009, **38**(1), 253–278.
17 T. W. Kim and K. S. Choi, Nanoporous $BiVO_4$ Photoanodes with Dual-Layer Oxygen Evolution Catalysts for Solar Water Splitting, *Science*, 2014, **343**(6174), 990–994.
18 P. Subramanyam, T. Khan, G. N. Sinha, D. Suryakala and C. Subrahmanyam, Plasmonic Bi nanoparticle decorated $BiVO_4$/rGO as an efficient photoanode for photoelectrochemical water splitting, *Int. J. Hydrogen Energy*, 2020, **45**(13), 7779–7787.
19 Z. Wang, Y. Wei, X. Wang, W. Zhang and J. Su, Plasmonic Au nanopraticles modified nanopyramid-arrays $BiVO_4$ with enhanced photoelectrochemical activity, *J. Electrochem. Soc.*, 2019, **166**(5), H3138.
20 J. H. Kim, J. W. Jang, H. J. Kang, G. Magesh, J. Y. Kim, J. H. Kim, J. Lee and J. S. Lee, Palladium oxide as a novel oxygen evolution catalyst on $BiVO_4$ photoanode for photoelectrochemical water splitting, *J. Catal.*, 2014, **317**, 126–134.
21 H. S. Han, S. Shin, D. H. Kim, I. J. Park, J. S. Kim, P. S. Huang, J. K. Lee, I. S. Cho and X. L. Zheng, Boosting the solar water oxidation performance of a $BiVO_4$ photoanode by crystallographic orientation control, *Energy Environ. Sci.*, 2018, **11**(5), 1299–1306.
22 C. W. Kim, Y. S. Son, M. J. Kang, D. Y. Kim and Y. S. Kang, (040)-Crystal Facet Engineering of $BiVO_4$ Plate Photoanodes for Solar Fuel Production, *Adv. Energy Mater.*, 2016, **6**(4), 1501754.
23 C. Lin, C. R. Dong, S. Kim, Y. Lu, Y. L. Wang, Z. Y. Yu, Y. Gu, Z. Y. Gu, D. K. Lee, K. Zhang and J. H. Park, Photo-Electrochemical Glycerol Conversion over a Mie Scattering Effect Enhanced Porous $BiVO_4$ Photoanode, *Adv. Mater.*, 2023, **35**(15), 2209955.
24 K. Sivula, Metal Oxide Photoelectrodes for Solar Fuel Production, Surface Traps, and Catalysis, *J. Phys. Chem. Lett.*, 2013, **4**(10), 1624–1633.
25 P. Guan, H. Y. Bai, F. G. Wang, H. Yu, D. B. Xu, W. Q. Fan and W. D. Shi, *In situ* anchoring Ag through organic polymer for configuring efficient plasmonic $BiVO_4$ photoanode, *Chem. Eng. J.*, 2019, **358**, 658–665.
26 W. W. Yang, Y. J. Xiong, L. L. Zou, Z. Q. Zou, D. D. Li, Q. X. Mi, Y. S. Wang and H. Yang, Plasmonic Pd Nanoparticle- and Plasmonic Pd Nanorod-Decorated $BiVO_4$ Electrodes with Enhanced Photoelectrochemical Water Splitting Efficiency Across Visible-NIR Region, *Nanoscale Res. Lett.*, 2016, **11**, 283.

27 R. Gutkowski, D. Peeters and W. Schuhmann, Improved photoelectrochemical performance of electrodeposited metal-doped $BiVO_4$ on Pt-nanoparticle modified FTO surfaces, *J. Mater. Chem. A*, 2016, **4**(20), 7875–7882.
28 Z. Z. Li and X. C. Meng, Recent development on palladium enhanced photocatalytic activity: A review, *J. Alloys Compd.*, 2020, **830**, 154669.
29 S. Sarkar and S. C. Peter, An overview on Pd-based electrocatalysts for the hydrogen evolution reaction, *Inorg. Chem. Front.*, 2018, **5**(9), 2060–2080.
30 M. Nishijima, M. Jo, Y. Kuwahara and M. Onchi, Electron energy loss spectra of a Pd (110) clean surface, *Solid State Commun.*, 1986, **58**(1), 75–77.
31 X. C. Meng, Z. Z. Li and Z. S. Zhang, Highly efficient degradation of phenol over a Pd-BiOBr Mott-Schottky plasmonic photocatalyst, *Mater. Res. Bull.*, 2018, **99**, 471–478.
32 X. C. Meng, Z. Z. Li and Z. S. Zhang, Palladium nanoparticles and rGO co-modified $BiVO_4$ with greatly improved visible light-induced photocatalytic activity, *Chemosphere*, 2018, **198**, 1–12.
33 X. C. Meng, Z. Z. Li and Z. S. Zhang, Pd-nanoparticle-decorated peanut-shaped $BiVO_4$ with improved visible light-driven photocatalytic activity comparable to that of TiO_2 under UV light, *J. Catal.*, 2017, **356**, 53–64.
34 T. Takayama, M. Sakai, S. Yamazoe and T. Komatsu, Durable Electrocatalytic CO_2 Reduction Using Intermetallic Compound PdIn Nanoparticles and Their Application to a Solar Energy Harvesting System, *ACS Appl. Energy Mater.*, 2023, **6**(5), 2793–2803.
35 A. A. Wilson, S. Corby, L. Francàs, J. R. Durrant and A. Kafizas, The effect of nanoparticulate PdO co-catalysts on the faradaic and light conversion efficiency of WO3 photoanodes for water oxidation, *Phys. Chem. Chem. Phys.*, 2021, **23**(2), 1285–1291.
36 A. J. Bard, *Standard Potentials in Aqueous Solution*, Routledge, 1st edn, 1985.
37 C. Burda, X. B. Chen, R. Narayanan and M. A. El-Sayed, Chemistry and properties of nanocrystals of different shapes, *Chem. Rev.*, 2005, **105**(4), 1025–1102.
38 G. V. Hartland, Optical Studies of Dynamics in Noble Metal Nanostructures, *Chem. Rev.*, 2011, **111**(6), 3858–3887.
39 C. Brissaud, L. V. Besteiro, J. Y. Piquemal and M. Comesaña-Hermo, Plasmonics: A Versatile Toolbox for Heterogeneous Photocatalysis, *Sol. RRL*, 2023, **7**(13), 2300195.
40 C. Clavero, Plasmon-induced hot-electron generation at nanoparticle/metal-oxide interfaces for photovoltaic and photocatalytic devices, *Nat. Photonics*, 2014, **8**(2), 95–103.
41 M. Ijaz, Plasmonic hot electrons: Potential candidates for improved photocatalytic hydrogen production, *Int. J. Hydrogen Energy*, 2023, **48**(26), 9609–9619.
42 H. Petek, M. J. Weida, H. Nagano and S. Ogawa, Real-time observation of adsorbate atom motion above a metal surface, *Science*, 2000, **288**(5470), 1402–1404.
43 B. N. J. Persson, Polarizability of Small Spherical Metal Particles - Influence of the Matrix Environment, *Surf. Sci.*, 1993, **281**(1–2), 153–162.
44 C. A. Mesa, L. Francàs, K. R. Yang, P. Garrido-Barros, E. Pasto, Y. M. Ma, A. Kafizas, T. E. Rosser, M. T. Mayer, E. Reisner, M. Grätzel, V. S. Batista and J. R. Durrant, Multihole water oxidation catalysis on haematite photoanodes revealed by operando spectroelectrochemistry and DFT, *Nat. Chem.*, 2020, **12**(1), 82–89.
45 Z. Meng, E. Pastor, S. Selim, H. Ning, M. Maimaris, A. Kafizas, J. R. Durrant and A. A. Bakulin, Operando IR Optical Control of Localized Charge Carriers in $BiVO_4$ Photoanodes, *J. Am. Chem. Soc.*, 2023, **145**(32), 17700–17709.
46 S. Selim, E. Pastor, M. García-Tecedor, M. R. Morris, L. Francàs, M. Sachs, B. Moss, S. Corby, C. A. Mesa, S. Gimenez, A. Kafizas, A. A. Bakulin and J. R. Durrant, Impact of Oxygen Vacancy Occupancy on Charge Carrier Dynamics in $BiVO_4$ Photoanodes, *J. Am. Chem. Soc.*, 2019, **141**(47), 18791–18798.
47 I. H. Van Stokkum, D. S. Larsen and R. Van Grondelle, Global and target analysis of time-resolved spectra, *Biochim. Biophys. Acta, Bioenerg.*, 2004, **1657**(2–3), 82–104.
48 C. Ruckebusch, M. Sliwa, P. D. Pernot, A. De Juan and R. Tauler, Comprehensive data analysis of femtosecond transient absorption spectra: A review, *J. Photochem. Photobiol., C*, 2012, **13**(1), 1–27.
49 T. Kong, A. Liao, Y. Xu, X. Qiao, H. Zhang, L. Zhang and C. Zhang, Recent advances and mechanism of plasmonic metal–semiconductor photocatalysis, *RSC Adv.*, 2024, **14**(24), 17041–17050.
50 Y. Miao and M. Shao, Photoelectrocatalysis for high-value-added chemicals production, *Chin. J. Catal.*, 2022, **43**(3), 595–610.
51 M. R. Anuar and A. Z. Abdullah, Challenges in biodiesel industry with regards to feedstock, environmental, social and sustainability issues: A critical review, *Renewable Sustainable Energy Rev.*, 2016, **58**, 208–223.
52 S. Verma, S. Lu and P. J. A. Kenis, Co-electrolysis of CO_2 and glycerol as a pathway to carbon chemicals with improved technoeconomics due to low electricity consumption, *Nat. Energy*, 2019, **4**(6), 466–474.
53 B. Mei, G. Mul and B. Seger, Beyond Water Splitting: Efficiencies of Photo-Electrochemical Devices Producing Hydrogen and Valuable Oxidation Products, *Adv. Sustainable Syst.*, 2017, **1**(1–2), 1600035.
54 G. Dodekatos, S. Schünemann and H. Tüysüz, Recent Advances in Thermo-, Photo-, and Electrocatalytic Glycerol Oxidation, *ACS Catal.*, 2018, **8**(7), 6301–6333.
55 L. F. Fan, B. W. Liu, X. Liu, N. Senthilkumar, G. X. Wang and Z. H. Wen, Recent Progress in Electrocatalytic Glycerol Oxidation, *Energy Technol.*, 2021, **9**(2), 2000804.
56 H. Luo, J. Barrio, N. Sunny, A. Li, L. Steier, N. Shah, I. E. Stephens and M. M. Titirici, Progress and perspectives in photo–and electrochemical–oxidation of biomass for sustainable chemicals and hydrogen production, *Adv. Energy Mater.*, 2021, **11**(43), 2101180.
57 B. Katryniok, H. Kimura, E. Skrzynska, J. S. Girardon, P. Fongarland, M. Capron, R. Ducoulombier, N. Mimura,

S. Paul and F. Dumeignil, Selective catalytic oxidation of glycerol: perspectives for high value chemicals, *Green Chem.*, 2011, **13**(8), 1960–1979.

58 J. L. Han, V. A. Soloshonok, K. D. Klika, J. Drabowicz and A. Wzorek, Chiral sulfoxides: advances in asymmetric synthesis and problems with the accurate determination of the stereochemical outcome, *Chem. Soc. Rev.*, 2018, **47**(4), 1307–1350.

59 P. Scherrer, Bestimmung der Grosse und inneren Struktur von Kolloidteilchen mittels Rontgenstrahlen, *Nachr. Ges. Wiss. Gottingen*, 1918, **2**, 8–100.

60 T. Lopes, L. Andrade, H. A. Ribeiro and A. Mendes, Characterization of photoelectrochemical cells for water splitting by electrochemical impedance spectroscopy, *Int. J. Hydrogen Energy*, 2010, **35**(20), 11601–11608.

61 M. O. Sergeev, A. A. Revina, S. A. Busev, V. I. Zolotarevskiy, K. N. Zhavoronkova and O. A. Boeva, Catalytic properties of monometallic and bimetallic palladium and rhodium nanoparticles obtained in reverse micellar systems, *Nanotechnol. Rev.*, 2014, **3**(5), 515–525.

62 A. Dewan, M. Sarmah, A. J. Thakur, P. Bharali and U. Bora, Greener Biogenic Approach for the Synthesis of Palladium Nanoparticles Using Papaya Peel: An Eco-Friendly Catalyst for C-C Coupling Reaction, *ACS Omega*, 2018, **3**(5), 5327–5335.

63 Y. Hayakawa, M. Furuya, H. Tahara, Y. Kosuge, T. Kimura, K. Sugawa and J. Otsuki, Modulation Technique of Localized Surface Plasmon Resonance of Palladium Nanospheres by Coating with Titanium Dioxide Shell for Application to Photothermal Therapy Agent, *Nanoscale Res. Lett.*, 2022, **17**(1), 60.

64 P. Brack, J. S. Sagu, T. N. Peiris, A. McInnes, M. Senili, K. U. Wijayantha, F. Marken and E. Selli, Aerosol–assisted CVD of bismuth vanadate thin films and their photoelectrochemical properties, *Chem. Vap. Deposition*, 2015, **21**(1–3), 41–45.

65 V. Torrisi, M. Censabella, G. Piccitto, G. Compagnini, M. G. Grimaldi and F. Ruffino, Characteristics of Pd and Pt nanoparticles produced by nanosecond laser irradiations of thin films deposited on topographically-structured transparent conductive oxides, *Coatings*, 2019, **9**(2), 68.

66 S. Yang, Y. Hou, B. Zhang, X. H. Yang, W. Q. Fang, H. J. Zhao and H. G. Yang, Highly efficient overlayer derived from peroxotitanium for dye-sensitized solar cells, *J. Mater. Chem. A*, 2013, **1**(4), 1374–1379.

67 K.-H. Su, Q.-H. Wei, X. Zhang, J. Mock, D. R. Smith and S. Schultz, Interparticle coupling effects on plasmon resonances of nanogold particles, *Nano Lett.*, 2003, **3**(8), 1087–1090.

68 S. Marhaba and S. E. Samad, Interparticle distance effect on the optical response of platinum dimer nanoparticles, *Chem. Afr.*, 2021, **4**(2), 477–482.

69 B. J. Trześniewski and W. A. Smith, Photocharged $BiVO_4$ photoanodes for improved solar water splitting, *J. Mater. Chem. A*, 2016, **4**(8), 2919–2926.

70 P. M. Rao, L. Cai, C. Liu, I. S. Cho, C. H. Lee, J. M. Weisse, P. Yang and X. Zheng, Simultaneously efficient light absorption and charge separation in $WO_3/BiVO_4$ core/shell nanowire photoanode for photoelectrochemical water oxidation, *Nano Lett.*, 2014, **14**(2), 1099–1105.

71 Y.-H. Wu, D. A. Kuznetsov, N. C. Pflug, A. Fedorov and C. R. Müller, Solar-driven valorisation of glycerol on $BiVO_4$ photoanodes: effect of co-catalyst and reaction media on reaction selectivity, *J. Mater. Chem. A*, 2021, **9**(10), 6252–6260.

72 L.-W. Huang, T.-G. Vo and C.-Y. Chiang, Converting glycerol aqueous solution to hydrogen energy and dihydroxyacetone by the $BiVO_4$ photoelectrochemical cell, *Electrochim. Acta*, 2019, **322**, 134725.

73 F. F. Abdi, A. Dabirian, B. Dam and R. Van De Krol, Plasmonic enhancement of the optical absorption and catalytic efficiency of $BiVO_4$ photoanodes decorated with Ag@ SiO_2 core–shell nanoparticles, *Phys. Chem. Chem. Phys.*, 2014, **16**(29), 15272–15277.

74 D. K. Bora, M. Nadjafi, A. Armutlulu, D. Hosseini, P. Castro-Fernández and R. Toth, Photoelectrochemical glycerol oxidation on Mo-$BiVO_4$ photoanodes shows high photocharging current density and enhanced H_2 evolution, *Energy Adv.*, 2022, **1**(10), 715–728.

75 G. D. Reid and K. Wynne, Ultrafast laser technology and spectroscopy, *Encycl. Anal. Chem.*, 2000, **35**(4), 13644–13670.

76 C. Manzoni, D. Polli and G. Cerullo, Two-color pump-probe system broadly tunable over the visible and the near infrared with sub-30 fs temporal resolution, *Rev. Sci. Instrum.*, 2006, **77**(2), 023103.

77 Y. M. Ma, S. R. Pendlebury, A. Reynal, F. Le Formal and J. R. Durrant, Dynamics of photogenerated holes in undoped $BiVO_4$ photoanodes for solar water oxidation, *Chem. Sci.*, 2014, **5**(8), 2964–2973.

78 N. Aiga, Q. Jia, K. Watanabe, A. Kudo, T. Sugimoto and Y. Matsumoto, Electron–phonon coupling dynamics at oxygen evolution sites of visible-light-driven photocatalyst: bismuth vanadate, *J. Phys. Chem. C*, 2013, **117**(19), 9881–9886.

79 A. Kahraman, M. B. Vishlaghi, I. Baylam, A. Sennaroglu and S. Kaya, Roles of charge carriers in the excited state dynamics of $BiVO_4$ photoanodes, *J. Phys. Chem. C*, 2019, **123**(47), 28576–28583.

80 J. Ravensbergen, F. F. Abdi, J. H. van Santen, R. N. Frese, B. Dam, R. van de Krol and J. T. M. Kennis, Unraveling the Carrier Dynamics of $BiVO_4$: A Femtosecond to Microsecond Transient Absorption Study, *J. Phys. Chem. C*, 2014, **118**(48), 27793–27800.

81 I. Grigioni, L. Ganzer, F. V. A. Camargo, B. Bozzini, G. Cerullo and E. Selli, In Operando Photoelectrochemical Femtosecond Transient Absorption Spectroscopy of $WO_3/BiVO_4$ Heterojunctions, *ACS Energy Lett.*, 2019, **4**(9), 2213–2219.

82 S. Link and M. A. El-Sayed, Spectral properties and relaxation dynamics of surface plasmon electronic oscillations in gold and silver nanodots and nanorods, *ACS Publ.*, 1999, **103**, 8410–8426.

83 K. Wu, W. E. Rodríguez-Córdoba, Y. Yang and T. Lian, Plasmon-induced hot electron transfer from the Au tip to CdS rod in CdS-Au nanoheterostructures, *Nano Lett.*, 2013, **13**(11), 5255–5263.

84 Y. Suzuki, D. H. Murthy, H. Matsuzaki, A. Furube, Q. Wang, T. Hisatomi, K. Domen and K. Seki, Rational interpretation of correlated kinetics of mobile and trapped charge carriers: analysis of ultrafast carrier dynamics in $BiVO_4$, *J. Phys. Chem. C*, 2017, **121**(35), 19044–19052.

85 L. Du, A. Furube, K. Yamamoto, K. Hara, R. Katoh and M. Tachiya, Plasmon-induced charge separation and recombination dynamics in gold – TiO_2 nanoparticle systems: dependence on TiO_2 particle size, *J. Phys. Chem. C*, 2009, **113**(16), 6454–6462.

86 P. Subramanyam, B. Meena, V. Biju, H. Misawa and S. Challapalli, Emerging materials for plasmon-assisted photoelectrochemical water splitting, *J. Photochem. Photobiol., C*, 2022, **51**, 100472.

87 A. Yamakata, C. S. K. Ranasinghe, N. Hayashi, K. Kato and J. J. M. Vequizo, Identification of individual electron-and hole-transfer kinetics at $CoO_x/BiVO_4/SnO_2$ double heterojunctions, *ACS Appl. Energy Mater.*, 2019, **3**(1), 1207–1214.

88 Y. Bai, C. Li, L. Liu, Y. Yamaguchi, M. Bahri, H. Yang, A. Gardner, M. A. Zwijnenburg, N. D. Browning, A. J. Cowan, A. Kudo, A. I. Cooper and R. S. Sprick, Photocatalytic overall water splitting under visible light enabled by a particulate conjugated polymer loaded with palladium and iridium, *Angew. Chem.*, 2022, **134**(26), e202201299.